Human Molecular Genetics, 2014, Vol. 23, No. 12 **3212–3227**
doi:10.1093/hmg/ddu031
Advance Access published on January 26, 2014

Germline disruption of Pten localization causes enhanced sex-dependent social motivation and increased glial production

Amanda K. Tilot[1,2,3], Mary K. Gaugler[2,3], Qi Yu[2,3], Todd Romigh[2,3], Wanfeng Yu[2,3], Robert H. Miller[7], Thomas W. Frazier II[1,2,4] and Charis Eng[1,2,3,5,6,8,9,*]

[1]Howard Hughes Medical Institute Molecular Medicine Program, Department of Molecular Medicine, Cleveland Clinic Lerner College of Medicine, [2]Genomic Medicine Institute, [3]Lerner Research Institute, [4]Center for Autism, Pediatric Institute, [5]Taussig Cancer Institute, [6]Stanley Shalom Zielony Institute of Nursing Excellence, Cleveland Clinic, Cleveland, OH 44195, USA, [7]Department of Neurosciences, [8]Department of Genetics and Genome Sciences, [9]CASE Comprehensive Cancer Center, Case Western Reserve University School of Medicine, Cleveland, OH 44106, USA

Received September 27, 2013; Revised and Accepted January 21, 2014

PTEN Hamartoma Tumor Syndrome (PHTS) is an autosomal-dominant genetic condition underlying a subset of autism spectrum disorder (ASD) with macrocephaly. Caused by germline mutations in *PTEN*, PHTS also causes increased risks of multiple cancers via dysregulation of the PI3K and MAPK signaling pathways. Conditional knockout models have shown that neural Pten regulates social behavior, proliferation and cell size. Although much is known about how the intracellular localization of PTEN regulates signaling in cancer cell lines, we know little of how PTEN localization influences normal brain physiology and behavior. To address this, we generated a germline knock-in mouse model of cytoplasm-predominant Pten and characterized its behavioral and cellular phenotypes. The homozygous *Pten^{m3m4}* mice have decreased total Pten levels including a specific drop in nuclear Pten and exhibit region-specific increases in brain weight. The *Pten^{m3m4}* model displays sex-specific increases in social motivation, poor balance and normal recognition memory—a profile reminiscent of some individuals with high functioning ASD. The cytoplasm-predominant protein caused cellular hypertrophy limited to the soma and led to increased NG2 cell proliferation and accumulation of glia. The animals also exhibit significant astrogliosis and microglial activation, indicating a neuroinflammatory phenotype. At the signaling level, *Pten^{m3m4}* mice show brain region-specific differences in Akt activation. These results demonstrate that differing alterations to the same autism-linked gene can cause distinct behavioral profiles. The *Pten^{m3m4}* model is the first murine model of inappropriately elevated social motivation in the context of normal cognition and may expand the range of autism-related behaviors replicated in animal models.

INTRODUCTION

Multiple case reports and prospective studies have linked autism spectrum disorder (ASD) in patients with severe macrocephaly to germline mutations in the *PTEN* gene (1–5). *PTEN* germline mutations occur in 7–27% of patients with ASD and macrocephaly and may account for up to 5% of all ASD cases as macrocephaly is found in ∼20% of the general ASD population (3,6,7). *PTEN* mutation screening is recommended in all cases of ASD where the individual has a head circumference greater than 3 standard deviations above the mean for their age and sex (8). Germline *PTEN* mutations cause subsets of several clinical syndromes known together as *PTEN* Hamartoma Tumor Syndrome (PHTS, OMIM #601728). In addition to ASD, developmental delay (DD) and Lhermitte–Duclos disease, PHTS can include neoplastic phenotypes such as macrocephaly and increased cancer risks, encompassed mainly by the clinical diagnosis of Cowden syndrome (1,3,9,10). A widely expressed phosphatase, PTEN is best known for dephosphorylating phosphatidylinositol(3,4,5)-triphosphate, inhibiting the PI3K/AKT/mTOR

*To whom correspondence should be addressed at: Genomic Medicine Institute, Cleveland Clinic, 9500 Euclid Avenue NE-50, Cleveland, OH 44195, USA. Tel: +1 2164443440; Fax: +1 2166360655; Email: engc@ccf.org

signaling pathway (11). Recent work using cancer cell lines indicates that PTEN functionality is partitioned by its subcellular localization; however, the impact of PTEN localization on its neurological functions is unknown.

Multiple murine models of increasing specificity established a role for *PTEN* in control of social behavior. At the germline, *Pten* heterozygosity causes decreased sociability in female mice (12). This phenotype persists when *Pten* loss is restricted to mature neurons or neuronal precursors, and such models also display decreased learning and increased anxiety (13–15). Although these and other gene-specific models mimic features of low-functioning ASD (decreased sociability and learning), there have yet to be genetic models replicating the more socially motivated profile of some high-functioning ASD patients (16,17).

Underlying these changes in social behavior is a multitude of cellular and molecular phenotypes caused by *PTEN* loss. Conditional knockouts and *in vitro* systems implicate neuronal Pten in the regulation of cell proliferation, soma size and dendritic arborization (15,18,19). Similarly, total loss of Pten in astrocytes causes hypertrophy and proliferation, while loss in oligodendrocytes causes hypermyelination without increased proliferation (20,21).

Studies from our group and others demonstrated the potential for PHTS-associated *PTEN* mutations to alter protein intracellular localization. By example, the K62R missense alteration produces a nuclear-predominant protein, while the K289E mutation leads to a cytoplasm-predominant PTEN (22,23). Somatic mutations in several regions of *PTEN* impacting protein localization also occur in sporadic cancers (22,24,25). Recent studies suggest the importance of PTEN subcellular localization in both PI3K and MAPK signaling inhibition, finding that MAPK inhibition is a nuclear function of PTEN in PHTS patient cell lines (25). Furthermore, nuclear PTEN dephosphorylates ERK1/2, leading to reduced cyclin D1 levels that promote G_0–G_1 cell cycle arrest (26,27). Although subcellular localization of PTEN has been studied *in vitro*, little is known about the role of PTEN localization *in vivo*.

We hypothesized that the intracellular localization of Pten contributes to control of social behavior and brain development. In this study, we address this hypothesis by interrogating a murine model where mislocalization of the full-length protein was created by germline knock-in missense mutations. We found that disrupting the nuclear/cytoplasmic balance of Pten in this fashion produces a behavioral profile distinct from conditional knockouts and reminiscent of a phenotype sometimes seen in high-functioning ASD. The pattern of preserved and altered Pten functions in the $Pten^{m3m4}$ model indicates the importance of nuclear/cytoplasmic partitioning in guiding *Pten*-regulated neural processes.

RESULTS

Alterations of body and brain growth in $Pten^{m3m4/m3m4}$ mice

We generated $Pten^{m3m4}$ mice by introducing five missense mutations into exon 7 of the mouse *Pten* gene via the cre-lox method (Fig. 1A). These mutations targeted the sequences analogous to the nuclear localization-like sequences found in the human *PTEN* gene. Mice were backcrossed onto the CD-1 outbred strain for at least five generations to reduce the impact of genetic heterogeneity on the results. Qualitative assessment of nuclear-cytoplasmic fractionated hemibrain protein revealed a dose-dependent decrease in the amounts of both nuclear and cytoplasmic Pten, with the $Pten^{m3m4/m3m4}$ bands displaying the lowest amount in each fraction ($n = 1$ mouse/genotype, Fig. 1B). Additionally, the ratio of nuclear to cytoplasmic Pten was lowest in the homozygous mutant condition. While Wt nuclear Pten was present at 93% of the cytoplasmic Pten level, the nuclear $Pten^{m3m4}$ protein was present at 72% of its cytoplasmic level. Fractionated protein isolated from cultured neurospheres showed a similar pattern of results, with homozygous mutant ($Pten^{m3m4/m3m4}$) mice showing the lowest level of cytoplasmic Pten combined with nearly absent nuclear Pten (Supplementary Material, Fig. S1A). The signal intensity for nuclear and cytoplasmic Pten differed significantly from Wt for both heterozygous ($Pten^{wt/m3m4}$) and $Pten^{m3m4/m3m4}$ animals (repeated measures ANOVA, compartment × genotype: $n = 2$–3 embryos/genotype, $F_{(2,4)} = 61.007$, $P = 0.001$; *post hoc* tests: Wt versus $Pten^{wt/m3m4}$, $P = 0.043$, Wt versus $Pten^{m3m4/m3m4}$, $P = 0.002$; Supplementary Material, Fig. S1B). The average ratio of nuclear Pten to cytoplasmic was similar in Wt and $Pten^{wt/m3m4}$ neurospheres (nuclear/cytoplasmic Pten signal intensity = 0.21 and 0.22, respectively), while the ratio for $Pten^{m3m4/m3m4}$ neurospheres was greatly diminished (0.014). The mutations did not significantly change *Pten* transcription, as measured in total RNA extracted from hemibrains (ANOVA, $n = 5$/group, $F_{(2,12)} = 0.078$, $P = 0.93$; Fig. 1C).

Gross examination revealed that the expression of the $Pten^{m3m4}$ protein affects body growth in a sex-dependent manner. At post-natal day 40 (P40), male $Pten^{m3m4/m3m4}$ mice are smaller than Wt male littermates, while female $Pten^{m3m4/m3m4}$ mice are of similar body weight [two-factor ANOVA, $n = 9$–12/group, $F_{(2,30)} = 4.77$, $P = 0.018$ (genotype), $F_{(1,30)} = 35.87$, $P < 0.001$ (sex), $F_{(2,30)} = 5.90$, $P = 0.008$ (genotype × sex); Fig. 1D and F]. $Pten^{wt/m3m4}$ mice are not significantly smaller than Wt littermates. We previously described the megalencephaly phenotype in the $Pten^{m3m4}$ animals and found that $Pten^{m3m4/m3m4}$ animals have brain weights double that of Wt animals, and that this brain growth is continuous (28). Further structural-level examination indicated that the cytoplasm-predominant $Pten^{m3m4}$ protein altered brain growth in a region-specific manner. Both male and female $Pten^{m3m4/m3m4}$ mice have larger cerebra (ANOVA, $n = 5$/group, $F_{(2,12)} = 11.57$, $P = 0.002$) and cerebella (ANOVA, $n = 5$/group, $F_{(2,12)} = 17.72$, $P < 0.001$; Fig. 1E and G), while the hippocampi are not enlarged (ANOVA, $n = 5$/group, $F_{(2,12)} = 1.84$, $P = 0.20$; Fig. 1E and G). These results suggest that germline changes to the expression and perhaps intracellular distribution of Pten can inhibit body growth in a sex-dependent manner, and stimulate brain growth in a region-specific manner.

Enhanced social motivation in male $Pten^{m3m4/m3m4}$ mice

Targeted *Pten* loss in multiple neuronal populations leads to regional overgrowth, and loss in adult neurons or neuronal progenitors leads to diminished social behavior in mice (14,15,19,29). To examine the possibility that the $Pten^{m3m4}$ mutation alters social behavior, we performed behavioral phenotyping focused on ASD-like behaviors. As ASD is four times as common in males as females, we looked for differences in

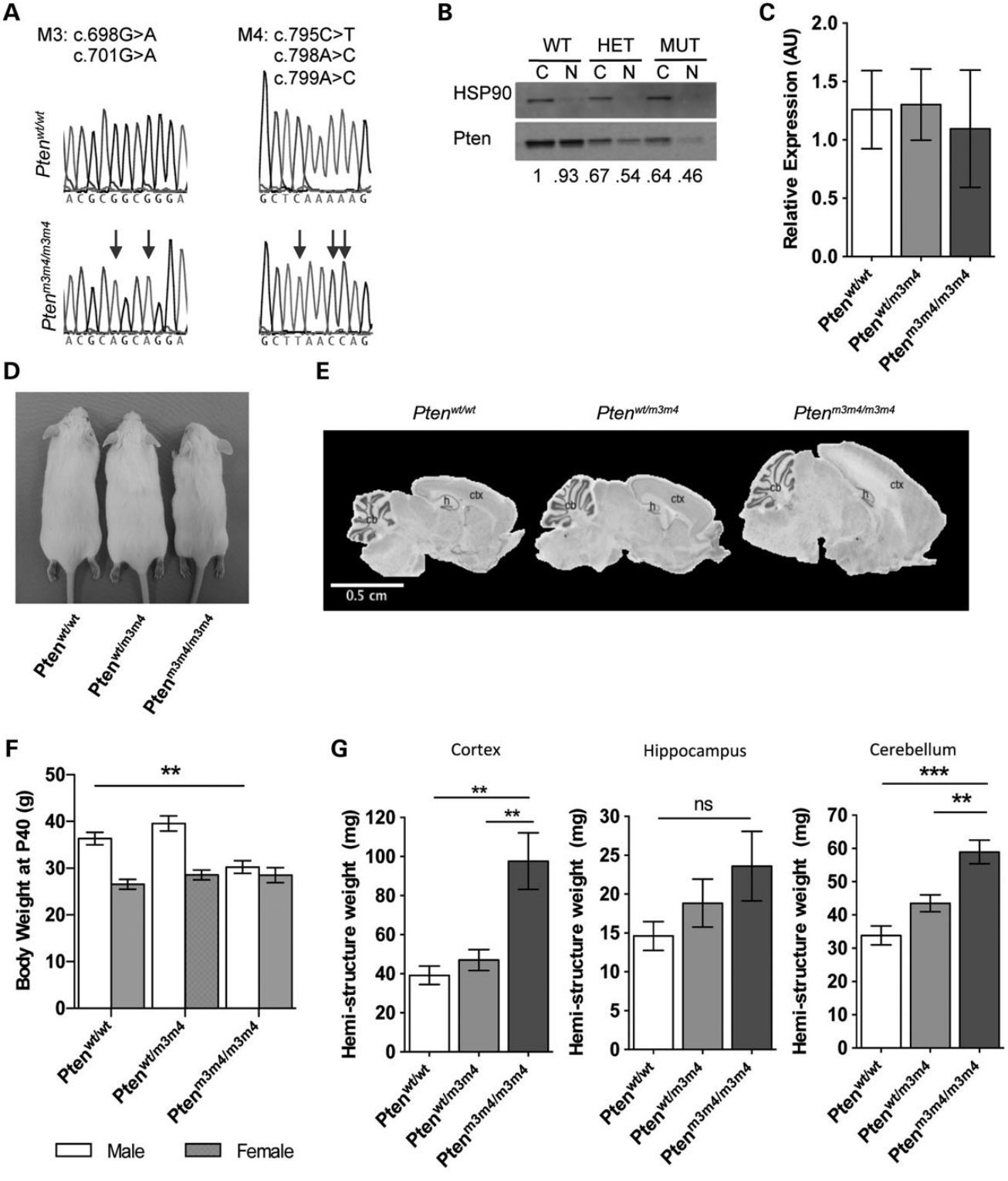

Figure 1. *Pten*^{m3m4} mice exhibit low nuclear Pten, sex-specific decreases in body weight and region-specific increases in brain weight. (**A**) Sequencing chromatograms indicating the five missense mutations comprising the *Pten*^{m3m4} alterations. The M3 mutations produce the amino acid substitutions p.R233Q and p.R234Q, while the M4 mutations cause the amino acid substitutions p.K266N and p.K267Q. (**B**) Western blot showing Pten levels in cytoplasmic (**C**) and nuclear (N) hemibrain lysates from three genotypes ($n = 1$ mouse/genotype). HSP90 is shown as a loading control, and Pten band quantification is shown below. (C) mRNA levels are not significantly altered in heterozygous or mutant mice. (**D**) Physical appearance of male *Pten*^{m3m4} mice at post-natal day 40. (**E**) Nissl stained sections showing overall brain morphology are shown for all three genotypes. (**F**) Average body weight of male and female *Pten*^{m3m4} mice at post-natal day 40. (**G**) Weight of cortex, hippocampus and cerebellum microdissected from one hemisphere of *Pten*^{m3m4} mice at post-natal day 40. $^{**}P < 0.01$, and $^{***}P < 0.001$ using Tukey's multiple comparison test.

social motivation between sexes in *Pten*^{m3m4} mice (30). The three-chamber social interaction test is a commonly used social behavior task and allows for assessment of both social motivation (preference trial) and preference for social novelty (memory trial). In the three-chamber task, *Pten*$^{m3m4/m3m4}$ animals were more variable in their preference for a social over non-social target (Levene's test: males = 7.21, $P = 0.005$, females = 4.46, $P = 0.019$). Male *Pten*$^{m3m4/m3m4}$ mice also showed greater variability in the memory trial (Levene's test: males = 3.65, $P = 0.048$, females = 2.91, $P = 0.069$). This increase in variability was specific to the three-chamber task, as the variance between groups did not differ in any other behavioral measure. Each genotype spent the greatest amount of time in the chamber containing the social target. Additionally, there were no differences between genotypes in the amount of time spent in the center chamber for either sex (ANOVA, males: $n = 6–8$ mice/genotype, $F_{(2,18)} = 1.37$, $P = 0.277$; females: $n = 10–15$ mice/genotype, $F_{(2,34)} = 2.38$, $P = 0.108$). To better account for a subset of male *Pten*^{m3m4} mice that showed a more extreme phenotype, we utilized nonlinear transformation and analyzed the three-chamber task data as ratios of time spent with one target over the other. In the preference trial, there was a trend toward male *Pten*$^{m3m4/m3m4}$ mice showing a greater preference for the social target over non-social, with female mutant animals behaving similarly to Wt (ANOVA, males: $n = 6–8$ mice/genotype, $F_{(2,18)} = 2.42$,

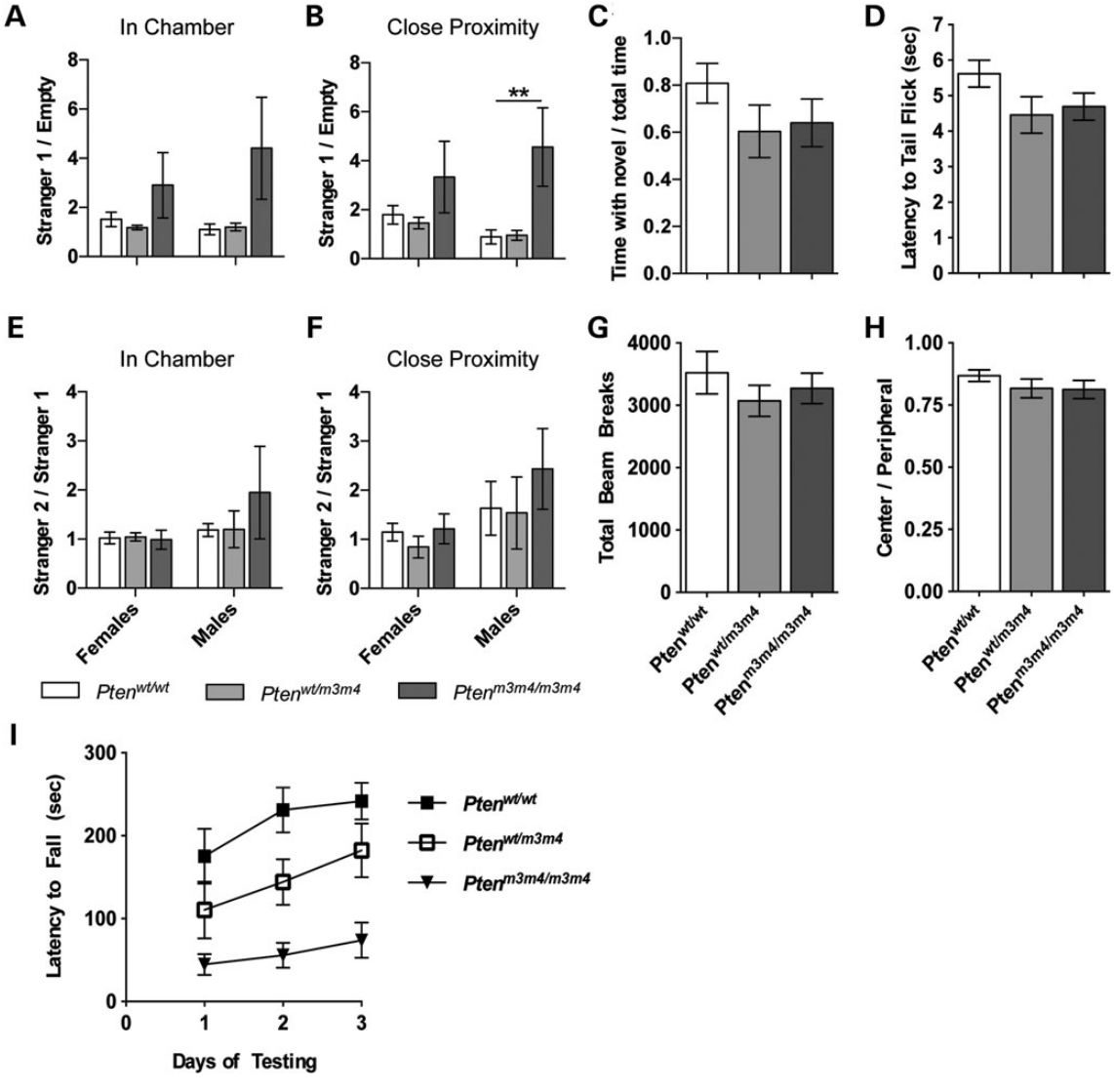

Figure 2. Male *Pten*^{m3m4} mice are hypersocial compared with Wt littermates, with no differences in recognition memory, anxiety or nociception. (**A**) Time spent in the chamber containing a social target over time spent in the empty chamber during the preference trial of the three-chamber task. (**B**) Time spent in close proximity to the social target over the non-social target during the same trials as in (A). (**C**) Recognition index (time spent with the novel object over time spent with either object) measured during the novel object recognition task. (**D**) Latency to tail flick during the nociception task. (**E**) Preference for social novelty measured by time spent in the chamber containing a novel social target (Stranger 2) compared with the familiar social target (Stranger 1). (**F**) Time spent in close proximity to Stranger 2 over Stranger 1 during the same trials as in (E). (**G**) Total locomotion in the open field, measured by total infrared beam breaks. (**H**) Number of beam breaks in the central area of the open field over breaks in the periphery. (**I**) Latency to fall (in seconds) during three consecutive days of accelerating rotarod training (average of three trials per day). $^{**}P = 0.01$ using Tukey's multiple comparison test.

$P = 0.117$; females: $n = 10–15$ mice/genotype, $F_{(2,34)} = 1.48$, $P = 0.24$; Fig. 2A). Our findings prompted examination of time spent in close proximity to the social or non-social target, where the test mouse is able to interact with the stimulus mouse. In this more refined measure, male *Pten*^{m3m4} mice showed a significantly greater preference for the social target over non-social (ANOVA, $n = 6–8$ mice/genotype, $F_{(2,18)} = 5.72$, $P = 0.013$, Fig. 2B). Female *Pten*^{m3m4} mice (ANOVA, $n = 10–15$ mice/genotype, $F_{(2,34)} = 1.42$, $P = 0.255$; Fig. 2B) and heterozygous animals of both sexes performed similarly to Wt.

In the memory trial of the three-chambered task, where test mice are exposed to the same social target as in the first trial as well as a second novel social target, both sexes of *Pten*$^{m3m4/m3m4}$ and *Pten*$^{wt/m3m4}$ mutant mice were indistinguishable from Wt in time spent in each chamber (ANOVA, males: $n = 6–8$ mice/genotype, $F_{(2,17)} = 0.641$, $P = 0.539$; females: $n = 10–15$ mice/genotype, $F_{(2,33)} = 0.41$, $P = 0.959$; Fig. 2E). Time spent in close interaction with the targets was also equivalent between genotypes (ANOVA, males: $n = 6–8$ mice/genotype, $F_{(2,17)} = 0.481$, $P = 0.626$; females: $n = 10–15$ mice/genotype, $F_{(2,32)} = 0.687$, $P = 0.51$; Fig. 2F). As in the preference trial, the genotypes did not differ in the amount of time spent in the center of the three-chamber apparatus (ANOVA, males: $n = 6–8$ mice/genotype, $F_{(2,18)} = 0.904$, $P = 0.423$; females: $n = 10–15$ mice/genotype, $F_{(2,34)} = 0.234$, $P = 0.79$). Together, these data indicate an increased social motivation profile in male *Pten*$^{m3m4/m3m4}$ mice compared with Wt.

Interpretation of the social behavior results requires additional behavioral phenotyping to identify any deficits that may influence performance in the three-chamber task. In order to identify recognition memory impairments that may influence the memory trial results, we performed a novel object recognition task with a 24-h delay using two different non-social objects. *Pten*$^{m3m4/m3m4}$ mice showed no deficit in recognition memory based on time spent with the novel object over the familiar (recognition index) (ANOVA, $n = 6–9$/genotype, $F_{(2,20)} = 1.31$, $P = 0.29$; Fig. 2C). Furthermore, total locomotion was measured using an open field apparatus with photobeam tracking, and the total number of beam breaks during the 30-min trial was similar across genotypes (ANOVA, $n = 5–12$/ genotype, $F_{(2,26)} = 0.4945$, $P = 0.62$; Fig. 2G). This indicates no impairment in ambulation that would impact performance on the three-chamber task. The enlarged cerebellum in the *Pten*$^{m3m4/m3m4}$ mice prompted testing of gross motor function and motor learning using the accelerating rotarod test. *Pten*$^{m3m4/m3m4}$ mice showed similar motor learning (improvement over 3 days of testing) to Wt (repeated measures ANOVA, $n = 7$/genotype, learning × genotype: $F_{(4,\ 36)} = 0.68$, $P = 0.61$; Fig. 2I). However, latency to fall remained significantly lower across all days, indicating poor balance in the *Pten*$^{m3m4/m3m4}$ animals (repeated measures ANOVA, $n = 7$/genotype, genotype: $F_{(2,18)} = 11.71$, $P = 0.001$; Fig. 2I).

We also examined whether changes in the intracellular distribution and expression levels of Pten alter anxiety and sensory perception, given that total Pten loss in adult neurons causes increased anxiety (15). To examine anxiety-like behavior in *Pten*^{m3m4} mice, we used open field photobeam data, and scored the number of beam breaks occurring in the center of the open field over breaks occurring on the periphery. Exploratory behavior (activity in the center of the field relative to periphery) was equal across genotypes (ANOVA, $n = 5–12$/genotype, $F_{(2,26)} = 0.87$, $P = 0.43$; Fig. 2H), indicating no differences in anxiety-like behavior with this task. To test the effect of the *Pten*^{m3m4} protein on sensory perception, we evaluated pain perception across genotypes using the heat-based tail-flick test. *Pten*$^{m3m4/m3m4}$ animals showed no difference in latency to tail flick when exposed to a halogen lamp (ANOVA, $n = 9$/genotype, $F_{(2,24)} = 2.05$, $P = 0.15$; Fig. 2D). No sex differences among genotypes were found for novel object recognition, tail flick, open field and rotarod tests (data not shown).

Taken together, these results indicate that male *Pten*$^{m3m4/m3m4}$ mice exhibit enhanced social motivation without alterations in recognition memory, anxiety or sensory perception. This suggests that changes in the intracellular distribution and expression level of Pten affect specific types of behavior, and drive changes that may be distinct from those caused by total Pten loss.

Pten^{m3m4} neurons display increased soma size without dendritic thickening

The altered social motivation in *Pten*$^{m3m4/m3m4}$ mice may result from alterations to neuronal cytoarchitecture, as cellular hypertrophy is a hallmark of total Pten loss (20,31). Ectopic growth of neuronal processes is also linked to *Pten* loss and is clearly observable in neurons within the molecular layer of the dentate gyrus (DG) (15). Therefore, we examined whether *Pten*$^{m3m4/m3m4}$ mice exhibit Pten-linked disruption of neuronal cytoarchitecture. Toward this end, we performed Golgi staining with brain tissue from P40 animals and measured soma size in cortical layer V pyramidal neurons, CA1 pyramidal neurons and granule cells of the DG and cerebellum. *Pten*$^{m3m4/m3m4}$ pyramidal cells of the cortex and hippocampus displayed 26% (ANOVA, $n = 204–254$ cells/genotype, $F_{(2,678)} = 29.69$, $P < 0.0001$; Fig. 3A and B) and 23% (ANOVA, $n = 93–141$ cells/genotype, $F_{(2,352)} = 27.42$, $P < 0.0001$; Fig. 3A and C) increases in soma size, respectively. We found a smaller difference in soma size within the DG granule cell population, with *Pten*$^{m3m4/m3m4}$ cells having a 10% larger cross-sectional area than Wt (ANOVA, $n = 130–204$ cells/genotype, $F_{(2,534)} = 4.46$, $P = 0.012$; Fig. 3A and D). Finally, we found no difference in the average soma size of cerebellar granule cells (ANOVA, $n = 50$ cells/genotype, $F_{(2,147)} = 1.42$, $P = 0.24$; Fig. 3A and E).

To determine whether these effects persist to the dendritic arbor, we measured dendritic diameter in secondary apical dendrites of CA1 pyramidal cell neurons. In contrast to our results in the soma, there was no difference in dendritic diameter across genotypes (ANOVA, $n = 57–61$ dendrites/genotype, $F_{(2,176)} = 0.47$, $P = 0.63$; Fig. 3A and G). Further examination of Golgi-stained tissue revealed no evidence for ectopic processes in the DG granule cells of homozygous or heterozygous animals (data not shown). Additionally, we did not observe any differences in the number of cerebellar granule cell processes (ANOVA, $n = 50$ cells/genotype, $F_{(2,147)} = 3.15$, $P = 0.046$, all *post hoc* comparisons non-significant, Fig. 3A and F), consistent with our finding in DG granule cells. No clear sex differences among genotypes were observed in the Golgi staining analyses, although a larger sample size would be required to confirm this finding (data not shown). These results suggest that the reduced level of cytoplasm-predominant

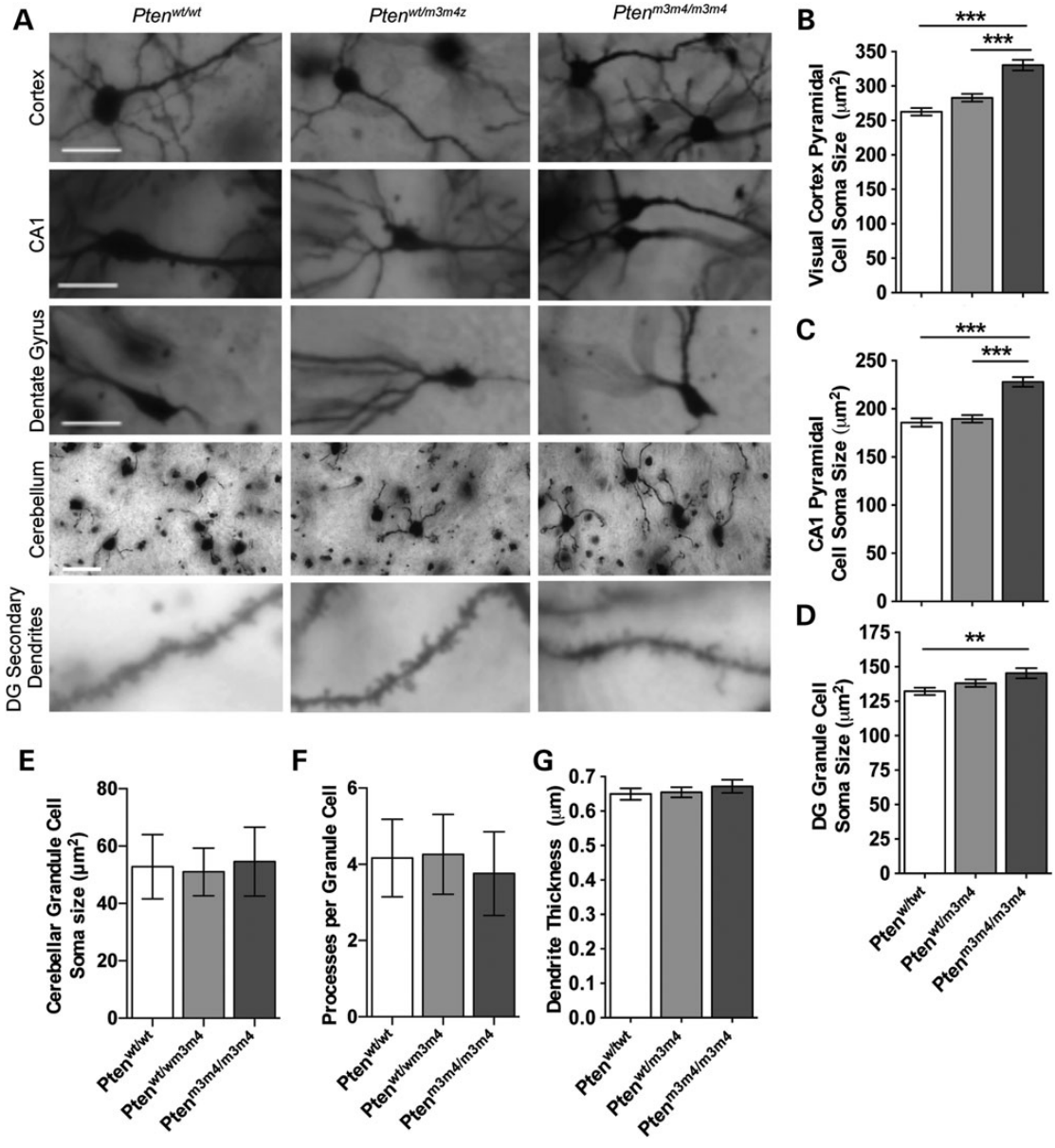

Figure 3. Variable cellular hypertrophy without changes in process number or thickness in *Pten*^{m3m4} mice at P40. (**A**) Representative images of (top row) cortical layer V pyramidal neurons, (second row) CA1 pyramidal neurons, (third row) DG granule neurons, (fourth row) cerebellar granule neurons, and secondary apical dendrites on CA1 pyramidal neurons across genotypes, scale bar equals 50 μm for all but the cerebellar granule neurons where it equals 25 μm. (**B**–**E**) Quantification of soma size in the cell types depicted in (A). (**F**) Quantification of the number of processes per cerebellar granule cell. (**G**) Quantification of dendritic thickness for the dendrite population presented in the bottom row of A. **indicates $P < 0.01$, and ***indicates $P < 0.001$ using Tukey's multiple comparison test.

Pten^{m3m4} protein causes observable hypertrophy near the nucleus, but is insufficient to drive morphological changes in distant processes.

Increased number of astrocytes and oligodendrocytes in the *Pten*$^{m3m4/m3m4}$ brain

The brain overgrowth in *Pten*$^{m3m4/m3m4}$ mice may be a result of increased numbers of specific cell types, which could contribute to changes in social behavior. The germline expression of the *Pten*^{m3m4} mutation makes such cell type-dependent alterations possible. To test this possibility, we used immunohistochemical analysis with neuronal and glial markers to examine the number of neurons and glial cells in P40 animals. In *Pten*$^{m3m4/m3m4}$ mice, we observed a trend toward fewer total cells per 100 μm^2 (Wt average = 127 cells/field, *Pten*$^{m3m4/m3m4}$ average = 106 cells/field; ANOVA, $n = 24–39$ visual fields/genotype, $F_{(2,76)} = 2.71$, $P = 0.073$). Based on this result, further cell count measurements were analyzed as the number of each specific cell type counted divided by the total number of cells in the visual field. We found that there were no differences in the percentage of cortical cells that were NeuN-positive neurons (ANOVA, $n = 5$ animals/genotype, $F_{(2,27)} = 0.67$, $P = 0.52$; Fig. 4A and B). In contrast, there were significant increases in the percentage of S100b-positive astrocytes (ANOVA, $n = 5$ animals/genotype, $F_{(2,20)} = 6.21$, $P = 0.008$; Fig. 4A and C),

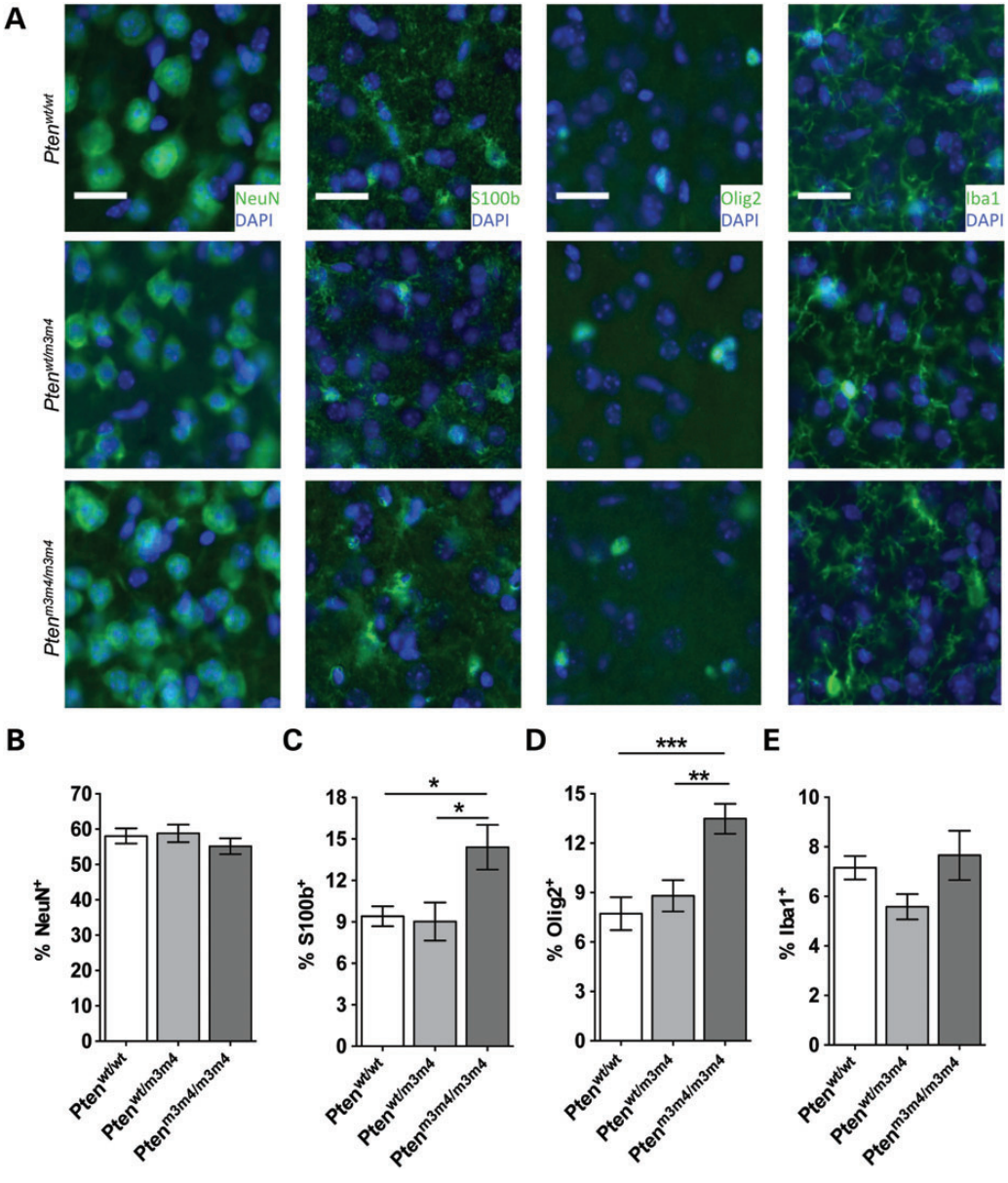

Figure 4. Increased numbers of astrocytes and oligodendrocytes in *Pten*^{m3m4} cortex at P40. (**A**) Representative images of cortical tissue sections immunostained with markers for (left to right, green) neurons (NeuN), astrocytes (S100b), oligodendrocytes (Olig2) and microglia (Iba1). Sections are counterstained with DAPI (blue) to illustrate nuclei. (**B**–**E**) Percentage of all cells counted that were positive for NeuN (**B**), S100b (**C**), Olig2 (**D**) or Iba1 (**E**). Scale bar equals 25 μm, *indicates $P < 0.05$, **indicates $P < 0.01$, and ***indicates $P < 0.001$ using Tukey's multiple comparison test.

and Olig2-positive oligodendrocytes (ANOVA $n = 5$ animals/genotype, $F_{(2,23)} = 10.42$, $P < 0.001$ Fig. 4A and D) in *Pten*$^{m3m4/m3m4}$ mice only. The presence of increased oligodendrocytes was confirmed with the oligodendrocyte marker CC1 (APC), as this antigen is not known to be increased in reactive astrocytes. To confirm that the counted cells were indeed oligodendrocytes, the tissue sections were also labeled with S100b, and CC1/S100b double-positive cells were not counted toward the total number of oligodendrocytes. This approach yielded more variable results than the Olig2 experiment; however, the direction of effect was the same with *Pten*$^{m3m4/m3m4}$ mice displaying a higher mean number of oligodendrocytes (data not shown). There were no differences among genotypes in the number of Iba1-positive microglia (ANOVA, $n = 5$ animals/genotype, $F_{(2,27)} = 2.57$, $P = 0.095$; Fig. 4A and E). These results suggest that alterations to Pten localization and expression via the *Pten*^{m3m4} mutation result in an increased number of astrocytes and oligodendrocytes, which may play roles in the increased brain growth and altered social behavior of *Pten*$^{m3m4/m3m4}$ mice.

Increased proliferation in cortex and hippocampus of *Pten*$^{m3m4/m3m4}$ mice

The increased numbers of astrocytes and oligodendrocytes led to the hypothesis that the increase in brain size in *Pten*$^{m3m4/m3m4}$ mice may be due to increased proliferation.

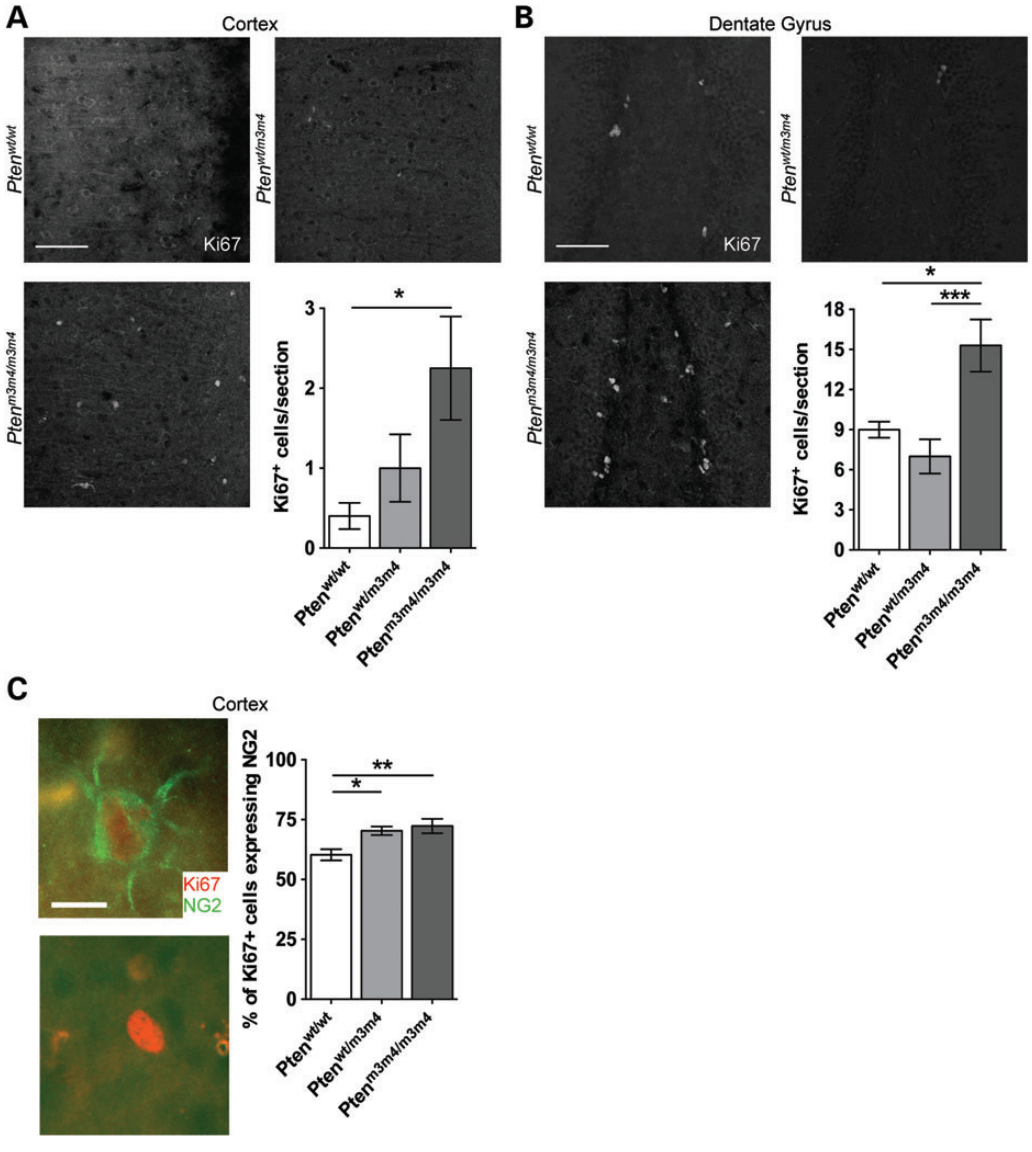

Figure 5. Increased proliferation in cortex and hippocampus of *Pten*^{m3m4} mice at P40. (**A**) Representative images of proliferating cells (Ki67, grey) in cortex. Quantification in lower right shows the number of Ki67-positive cells per image. (**B**) Representative images of proliferating cells (Ki67, grey) in DG. Quantification in lower right shows the number of Ki67-positive cells per image. (**C**) Representative images of cells positive for both Ki67 (red) and NG2 (green) (above), or Ki67 alone (below), with quantification of the percentage cortical Ki67+ cells that were also NG2+. Scale bar equals 50 μm in (A) and (B) and 10 μm in (C). *indicates $P < 0.05$, **indicates $P < 0.01$ and ***indicates $P < 0.001$ using Tukey's multiple comparison test.

To address this hypothesis, we utilized immunohistochemical staining with the proliferation marker Ki67 to determine proliferative activity in both cerebral cortex and hippocampus at P40. The number of Ki67-positive cells in both cortex (ANOVA, $n = 5$ animals/genotype, $F_{(2,25)} = 4.63$, $P = 0.02$; Fig. 5A) and DG (ANOVA, $n = 5$ animals/genotype, $F_{(2,26)} = 9.36$, $P < 0.001$; Fig. 5B) of *Pten*$^{m3m4/m3m4}$ animals was increased by 5.6- and 1.7-fold, respectively. Consistent with the unchanged ratios of astrocytes and oligodendrocytes, the number of Ki67-positive cells in both cortex and dentrate gyrus of *Pten*$^{wt/m3m4}$ mice were the same as Wt. The results suggest that expression of the Pten^{m3m4} protein enhances the proliferation of glial cells (astrocytes and oligodendrocytes), leading to enlargement of the *Pten*$^{m3m4/m3m4}$ brain.

Based on these findings, we hypothesized that the Ki67-positive population in the *Pten*$^{m3m4/m3m4}$ brain may include more NG2-positive polydendrocytes than Wt brain. We utilized NG2/Ki67 double labeling to determine the percentage of Ki67-positive cells in the cortex that were also positive for NG2. This percentage was higher in *Pten*$^{m3m4/m3m4}$ (78%) and *Pten*$^{wt/m3m4}$ (70%) brains than in Wt (60%) (ANOVA, $n = 6$–7 sections/genotype totaling > 125 cells/genotype, $F_{(2,27)} = 6.75$, $P = 0.007$; Fig. 5C). Taken together with the increase in total proliferation within the cortex, it suggests a multi-fold increase in the number of proliferating NG2 cells in the *Pten*$^{m3m4/m3m4}$ brain. This result supports our findings of increased oligodendrocytes and proliferating cells within the cortex, by demonstrating that the polydendrocyte population is hyperproliferative in the *Pten*$^{m3m4/m3m4}$ brain.

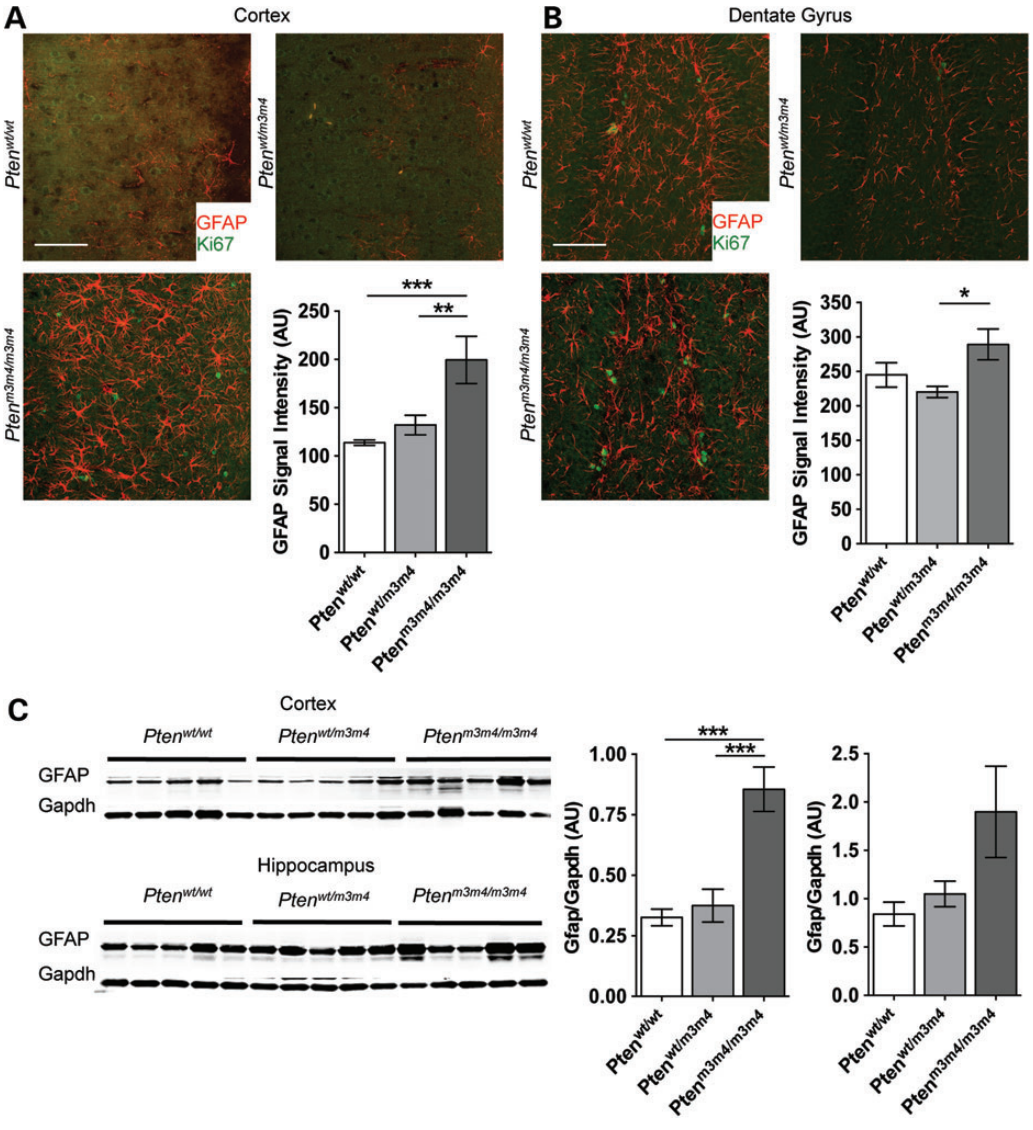

Figure 6. Reactive astrogliosis in cortex and hippocampus of *Pten*^{m3m4} mice at P40. (**A**) Representative images of reactive astrocytes (GFAP, red), and proliferating cells (Ki67, green) in cortex. Quantification in lower right shows intensity of GFAP immunostaining per image. (**B**) Representative images of reactive astrocytes (GFAP, red), and proliferating cells (Ki67, green) in DG. Quantification in lower right shows intensity of GFAP immunostaining per image. (**C**) Western blot showing GFAP expression in cortical and hippocampal lysates from P40 animals, with quantification of GFAP band intensity for both regions. Scale bar equals 50 μm, *indicates $P < 0.05$, **indicates $P < 0.01$ and ***indicates $P < 0.001$ using Tukey's multiple comparison test.

Reactive astrogliosis and microglial activation in *Pten*$^{m3m4/m3m4}$ mice

Our observations so far suggested the hypothesis that the increased astrocyte number in *Pten*$^{m3m4/m3m4}$ mice may occur as part of reactive astrogliosis. We began to address this hypothesis by using the astrogliosis-sensitive marker GFAP. *Pten*$^{m3m4/m3m4}$ mice displayed significantly increased GFAP-immunostaining throughout the cortex (ANOVA, $n = 5$ animals/genotype, $F_{(2,26)} = 9.28$ $P < 0.001$; Fig. 6A) and trended toward an increase in the DG (ANOVA, $F_{(2,27)} = 4.116$, $P = 0.023$; Tukey's multiple comparison test, Wt versus *Pten*$^{m3m4/m3m4}$, $P > 0.05$; Fig. 6B). In contrast, *Pten*$^{wt/m3m4}$ animals did not exhibit any increase in GFAP-immunostaining. Quantification of western blotting with cortical and hippocampal protein lysates confirmed the significant increases in the GFAP band intensity in *Pten*$^{m3m4/m3m4}$ brains (Fig. 6C). To determine the extent of the astrogliosis, we looked for evidence of proliferating reactive astrocytes (GFAP+, Ki67+). We did not observe such double-labeled cells in either region (Fig. 6A and B), and additional analysis with S100b and Ki67 confirmed these results (data not shown). Together, these findings suggest that astrocyte proliferation is not likely to be a major contributor to the increased proliferation within the *Pten*^{m3m4} brain.

The increases in astrocyte GFAP expression in the cortex suggested a neuroinflammatory response in the *Pten*$^{m3m4/m3m4}$ brain. To test this possibility, we examined whether *Pten*$^{m3m4/m3m4}$ microglia exhibit an activated phenotype. In the *Pten*$^{m3m4/m3m4}$ cerebral cortex and hippocampus, the Iba1-positive microglia displayed thicker processes and enlarged cell bodies relative to

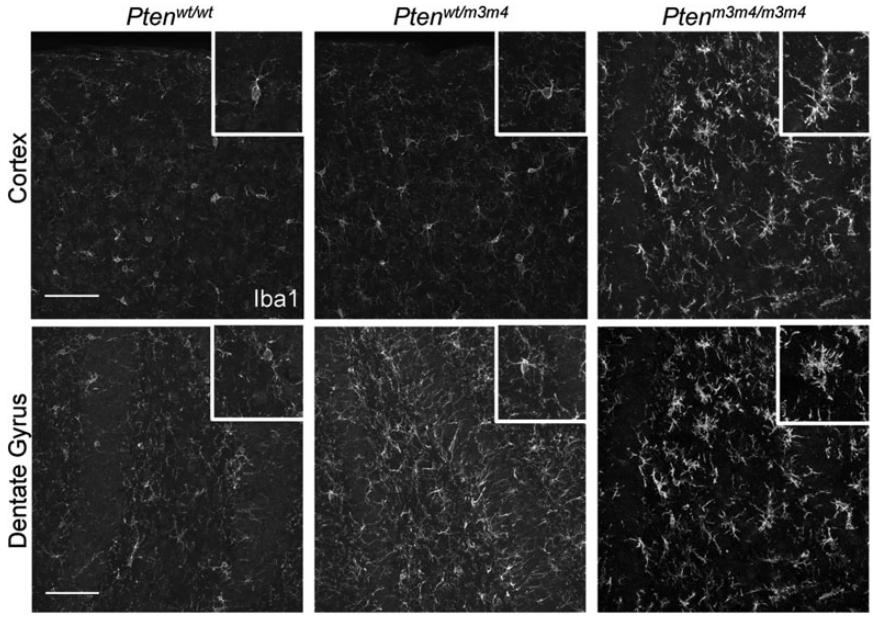

Figure 7. Morphology of activated microglia in cortex and dentate gyus of *Pten*^{m3m4} mice at P40. Representative images of microglia (Iba1, grey) in cortex. One representative cell is shown enlarged in the upper right of each panel. Scale bar equals 50 μm.

Wt and *Pten*$^{wt/m3m4}$ littermates, indicating a reactive state (Fig. 7). These results, combined with the reactive astrogliosis, indicate an elevated neuroinflammatory response in the *Pten*$^{m3m4/m3m4}$ brain.

Region-specific alterations to Pten signaling in the *Pten*$^{m3m4/m3m4}$ brain

The impact of changes to the intracellular distribution and expression level of Pten on glial proliferation and the neuroinflammatory response is largely unknown. However, aspects of Pten signaling are well understood from different vantage points. Cytoplasmic PTEN is best known in both cancer and neurobiology for negatively regulating the PI3K pathway, resulting in decreased phosphorylated-AKT (15,26). In cancer cell lines, nuclear PTEN negatively regulates MAPK signaling by decreasing levels of phosphorylated-ERK1/2 (26). Using western blotting, we examined whether *Pten*$^{m3m4/m3m4}$ brains exhibit elevated phosphorylated-Akt (Ser473) and/or phosphorylated-Erk1/2 (Thr202/Tyr204). The total amount of Pten protein was reduced by 44% in cerebra, 64% in hippocampus and 52% in cerebella of *Pten*$^{m3m4/m3m4}$ animals (Fig. 8A–C), in keeping with the diminished cytoplasmic, and nearly absent nuclear Pten levels (Fig. 1B, Supplementary Material, Fig. S1A and B). Interestingly, phosphorylated-Akt (Ser473) was only significantly elevated in cortex (Kruskal–Wallis test, $n = 3–5$ animals/genotype, $H = 8.57$, $P = 0.0013$; Dunn's multiple comparison test, Wt versus *Pten*$^{m3m4/m3m4}$, $P = 0.0071$; Fig. 8A). Phosphorylated-Erk1/2 was not significantly increased in any brain region examined from *Pten*$^{wt/m3m4}$ or *Pten*$^{m3m4/m3m4}$ mice. These results indicate that germline changes to the intracellular distribution and expression of Pten via the *Pten*^{m3m4} mutation produce brain region-specific elevations in phosphorylated-Akt and only mild changes in phosphorylated-Erk1/2. Given the well-understood impact of upregulated Akt signaling on proliferation across cell types, it is likely that the increases in phosphorylated-Akt are promoting glial proliferation and subsequent enlargement of the *Pten*$^{m3m4/m3m4}$ brain.

DISCUSSION

We have shown that Pten disruption-based protein mislocalization and haploinsufficiency results in abnormal social behavior and brain development. The resulting mouse model, *Pten*^{m3m4}, displays region-specific brain enlargement combined with sex-specific decreases in overall body size (Fig. 1A–G). Behaviorally, male *Pten*$^{m3m4/m3m4}$ mice exhibit increased social motivation and impaired balance, amidst an otherwise normal behavioral profile (Fig. 2A–I). Analysis of Golgi stained tissue sections revealed variable increases in soma size across neuronal populations, without changes in dendritic diameter or process number. Although Pten mislocalization does not affect neuron number (Fig. 4A and B), *Pten*$^{m3m4/m3m4}$ mice show increased production of astrocytes and oligodendrocytes (Fig. 4A, C and D). This result was supported by increases in the number of proliferating NG2 cells (Fig. 5A–C). Further examination of the *Pten*^{m3m4} astrocytes revealed reactive astrogliosis (Fig. 6A–C), an inflammatory phenotype supported by changes in microglial morphology (Fig. 7). Activation of Akt and Erk1/2, key Pten signaling proteins, was mild and variable across mice within a genotype, underscoring the complexity of the cell and behavioral phenotypes (Fig. 8A–C).

In 1979, Wing and Gould (16) described a subtype of ASD social interaction they termed 'active-but-odd'. These individuals are more likely to have been classified as having Asperger syndrome or high functioning autism and show increased but highly inappropriate social approach behaviors (e.g. decreased social distance, absence of conversational turn-taking) with

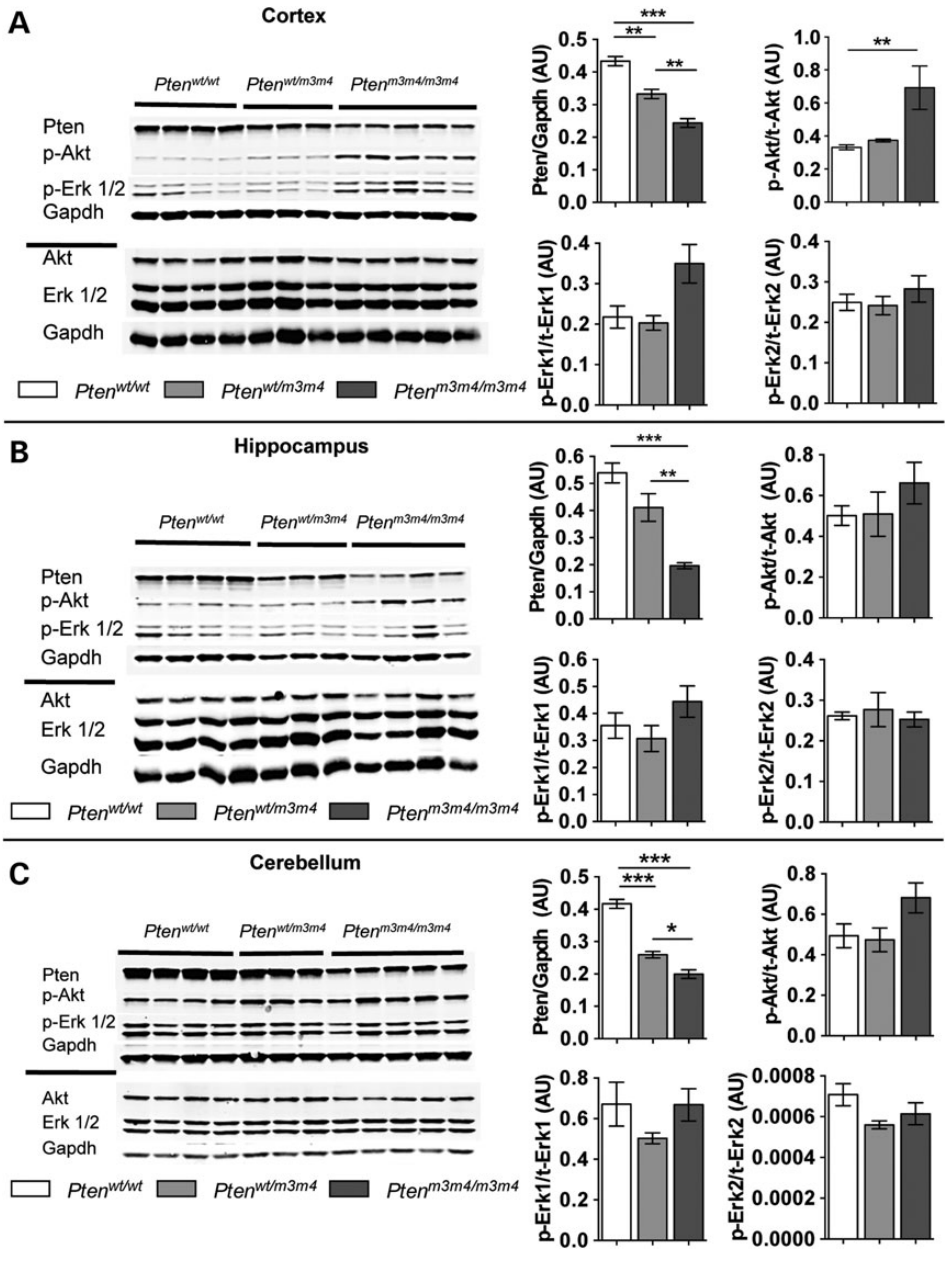

Figure 8. Decreased Pten leads to brain region-specific increases in phosphorylated-Akt and -Erk1/2 in *Pten*^{m3m4} mice. (**A**–**C**) Western blot showing Pten, phosphorylated (Ser473) and total Akt, phosphorylated (Thr202/Tyr204) and total Erk1/2 in (A) cortex, (B) hippocampus, and (C) cerebellum. Quantification of band intensity for each target protein is shown to the right of the western images. *indicates $P < 0.05$, **indicates $P < 0.01$, and ***indicates $P < 0.001$ using Tukey's or Dunn's multiple comparison tests.

average to above average intelligence and memory (16,17). The *Pten*^{m3m4} model is the first animal model of a syndromic autism exhibiting sex-specific increases in social motivation in the context of normal learning and memory. Following further phenotype analysis, this model may broaden the range of human social phenotypes that can be replicated in mice.

Previous reports using the three-chamber task focused on models exhibiting decreases in social motivation, manifesting in reduced interaction with the social target relative to control animals (12,15). Social behavior in humans is a continuous trait, and we applied this concept to the analysis of the three-chamber task (32). This is a novel interpretation of what the assay can detect, as prior usage assumes only the capacity to detect the absence of social behavior (33). Additionally, our interpretation of the test emphasizes time spent in close proximity to the social and non-social targets, as this more fine-grained measure better distinguishes meaningful social interaction than examining time spent in the entire chamber (33). This analysis, while a departure from standard methods, reveals increased in social motivation in the male *Pten*$^{m3m4/m3m4}$ mice that was less apparent when using the rougher measure of time spent in the entire social or non-social chamber.

Although our finding was unexpected, sex-specific decreases in social motivation were also reported in the *Pten*$^{+/-}$ model, where only female animals displayed decreased social behavior in the three-chamber task (12). Our finding supports the need for more fine-tuned behavioral analysis, and the sex-differences observed in this report will be the focus of future studies. Tests focused on the quality of the social interactions performed by *Pten*^{m3m4} mice are necessary to understand the purpose of the increased time spent with the social target. Additionally, the three-chamber task could be modified to use male *Pten*^{m3m4} animals as stimulus mice, to determine whether Wt mice show any avoidance behavior toward an animal with altered social interaction patterns.

At a molecular level, the increase in social motivation seen in male *Pten*^{m3m4} mice occurs despite elevated Akt signaling in the cortex (Fig. 8A), a signaling pathway implicated in the decreased sociability of *Pten* conditional knockouts (12,14,15,29). *Pten*^{m3m4} mice do have lower Pten dosage (Figs 1B and 8A–C, Supplementary Material, Fig. S1A and B), but the increased social motivation phenotype may be less related to this decrease, as female *Pten*$^{+/-}$ mice exhibit decreased social behavior (12). Thus, Pten localization may regulate pathways that affect social behavior independently from dosage alone, suggesting that mislocalization could promote different social motivation phenotypes. One could speculate that this social behavior phenotype may result from increased numbers of astrocytes and oligodendrocytes, as both cell types support synaptic function. Synaptic activity differences occur in children with ASD, and further work is needed to clarify the impact of altered cell-type ratios on synaptic function in this model.

Pten$^{m3m4/m3m4}$ mice also exhibited reduced balance (Fig. 2I), without differences in overall locomotion (Fig. 2G), indicating cerebellar dysfunction. Motor deficits relating to cerebellar function occur in ASD and in human PHTS, independently of ASD phenotypes (1,34,35), and difficulty with both executive function and fine motor tasks is observed in adults with PHTS (35,36). More broadly, motor difficulties and clumsiness are noted as frequent comorbidities in children with the 'active-but-odd' subtype of ASD social behavior (37). Finally, the lack of recognition memory impairment (Fig. 2C) also aligns with a model of high functioning or 'active-but-odd' ASD, as these subgroups show less cognitive impairment (38,39). One limitation to the behavioral analysis is the difference in background strain between *Pten*^{m3m4} mice and previous *Pten* models that are based on the inbred C57/BL6 genetic background (15). However, the outbred CD-1 background also offers advantages for the study of human disease. For example, behavioral phenotypes in this model are more striking given the increased genetic variability between animals.

The modest changes in neuronal cytoarchitecture in *Pten*$^{m3m4/m3m4}$ mice are noteworthy compared with the robust hypertrophy of both soma and dendrites, loss of cell polarity and increased dendritic spine density observed in other *Pten* models (15,20). The somata of cortical and CA1 pyramidal neurons were the most enlarged in this study, with dentate granule neurons being less effected, and cerebellar granule cells unchanged. We also observed no change in dendritic thickness or evidence of ectopic processes in the dentate granule neurons. Similarly, *Pten*^{m3m4} cerebellar granule cells exhibited no change in process number (Fig. 3). These results suggest that regulation of cell morphology is relatively Pten dose dependent, and that the morphology of distant processes may be more dependent on the activity of cytoplasmic Pten than nuclear Pten. Supporting the hypothesis that cytosolic Pten regulates cell size, treatment with the mTORC1 inhibitor rapamycin led to a reduction of neuronal hypertrophy in the *Nse-Cre;Pten*$^{loxP/loxP}$ model (13). This link between Pten and neuronal size is highly sensitive, as hypertrophy can occur as early as 14 days after *Pten* knockdown (40). Interestingly, Sperow *et al*. (41) report that Pten regulation of cell size is separate from its role in synaptic regulation, finding electrophysiologic changes prior to changes in neuronal morphology. Their results align with our findings of behavioral abnormalities in the presence of relatively normal cytoarchitecture. We should note that tissue from both male and female mice was used in the Golgi staining and other histological studies. Future studies are needed to understand the cellular and molecular alterations that give rise to the observed sex differences in body weight and social behavior, as such analyses would be underpowered at present.

This is the first report of Pten disruption, specifically of intracellular localization, causing increased numbers of oligodendrocytes and, combined with astrocytes, this overproduction of glia may contribute substantially to the increased brain size of *Pten*$^{m3m4/m3m4}$ mice (Fig. 4A, C, D). The trend toward reduced cell density in cortex may be explained by the increases in cell size, as larger cells may require greater intercellular distances to maintain appropriate contacts and communication (Fig. 3A and B). As the increase in glial production appears greater than the increase in cell size, we believe that the overall increase in brain size is due in larger part to greater numbers of glia. A causative role for glial production is supported by the increase in proliferation observed in both the cortex and hippocampus of *Pten*$^{m3m4/m3m4}$ mice (Fig. 5A and B). Previous reports show that either *Pten* loss or constitutively active Akt within oligodendrocytes produces hypermyelination, but no change in oligodendrocyte number (21,42). As both the Mapk and mTor signaling pathways have distinct roles in oligodendrocyte maturation, work is needed to uncover how germline disruption to both pathways through reduction in Pten dosage impacts oligodendrocyte production and maturation (43). Pten loss in neural precursors causes both hypertrophy and hyperproliferation of astrocytes and neurons *in vivo*, which contribute to increased brain size in the *Gfap-Cre* transgenic model (20,44). Specifically, Pten regulates radial glia-like precursors, and its loss drives terminal astrocyte proliferation (44). In the cortex (Fig. 8A), our findings may be due to either reduced Akt or Mapk regulation, which could promote increased proliferation (26). Within the hippocampus, the hyperproliferation phenotype is more likely due to mild Akt activation (Fig. 8B), although further studies would be required to confirm this hypothesis.

Further examination of *Pten*^{m3m4} astrocytes revealed significant astrogliosis at P40, supported by increased GFAP expression (Fig. 6A–C). Additional evidence for a neuroinflammatory phenotype in *Pten*$^{m3m4/m3m4}$ mice comes from the altered microglial morphology (Fig. 7). Interestingly, the GFAP-positive astrocyte population does not appear to be proliferative, indicating that the astrogliosis phenotype is not sufficiently severe to promote astrocyte proliferation (45). Rather, it is possible that in the context of this particular *Pten* mutation that increased

NG2-cell proliferation promotes increases in both oligodendrocytes and astrocytes, as this pluripotency is observed *in vitro* as well as in perturbed systems, such as the *shiverer* mouse model (46,47). In a previous study, neuronal loss of NF1 led to increased phospho-Erk expression in neurons and moderate astrogliosis that was not accompanied by astrocyte proliferation (48). Several reports demonstrate increased microglial activation in the brains of people with ASD, and together with our results, these data support the study of neuroinflammation in cases of ASD with PHTS (49,50).

It is the combined effects of the $Pten^{m3m4}$ mutation on every cell type that generates the behavioral phenotypes seen in this model, reflecting the genetic nature of syndromic autisms. *PTEN* mutations observed in PHTS patients with ASDs or DD were less likely to disrupt PI3K antagonization than *PTEN* mutations observed only in PHTS patients without ASD or DD (51). Similarly, a functional study of a single missense *PTEN* mutation associated with ASD showed only slightly diminished phosphatase activity despite increased membrane association in a glioblastoma cell line (52). These reports confirm the need to study how PTEN functions beyond PI3K antagonism regulate social behavior and to specifically identify how missense mutations alter these non-canonical functions.

In conclusion, we have shown that the impact of Pten on behavior and brain physiology depends on protein localization as well as dosage. These results add significant nuance to the roles of *Pten* in the CNS, demonstrating for the first time *in vivo* the importance of Pten subcellular localization in the regulation of proliferation, cell size, polarity and behavior. Our approach brings genetic models for ASD within PHTS closer to the human syndrome by constitutionally disrupting important functional aspects of the Pten protein. Our results highlight the importance of germline and functionally relevant genetic alterations in animal models of syndromic autisms, both as models of human disease and predictors of therapeutic efficacy.

MATERIALS AND METHODS

Animals

We used a standard homologous recombination method to generate a *Pten-m3m4* knock-in mouse. The segment of murine *Pten* exon 7 altered via knock-in is analogous to a section of human *PTEN* spanning exons 7–8. In human *in vitro* systems, inactivating two of the four nuclear localization sequence-like sequences (NLS) is required for disrupting proper subcellular localization of PTEN (27). The $Pten^{m3m4}$ targeting vector was electroporated into embryonic stem (ES) cells from the CD-1 genetic background (Charles River Laboratories International, Wilmington, MA, USA). Targeting (Site directed mutagenesis kit, Stratagene, La Jolla, CA, USA) resulted in introduction of five missense mutations within NLS3 and NLS4 (Fig. 1A), and the presence of a neomycin resistance cassette within the exon 7–8 intronic space. All final targeting vectors were verified by restriction digestion with multiple enzymes and direct DNA sequencing using the Sanger method (ABI 3730xl). Recombinant ES cells were injected into 129Sv/J blastocysts and transferred to a pseudopregnant female mouse. 129Sv/J;CD-1 chimeric animals were crossed with wild-type CD-1 mice to generate $Pten^{wt/m3m4}$ progeny. The knock-in $Pten^{m3m4}$ mutation was confirmed by sequencing tail DNA samples from the agouti offspring. $Pten^{wt/m3m4}$ mice were backcrossed with Wt CD-1 for at least five generations, and animals used in these experiments were littermates generated through $Pten^{wt/m3m4}$ crosses. Both male and female animals were used in all experiments.

All experiments were conducted under protocols approved by the Institutional Animal Care and Use Committee at Cleveland Clinic. Mice were maintained on a 14 : 10 light:dark cycle with access to food and water *ad libitum*. The room temperature was maintained between 18 and 26°C. Animals were killed via CO_2 asphyxiation or exsanguination via transcardial perfusion with phosphate-buffered saline (PBS).

Western blotting

In Figure 1B, fractionated protein samples were obtained from hemibrain tissue lysates using the NE-PER system (Thermo Scientific, Rockland, IL, USA), and 15 μg was used per sample in western blotting. Total protein samples used in Figure 8 were extracted from mouse brain tissue using RIPA buffer according to the standard protocols. For Pten pathway analysis, 30 μg of purified protein per sample was run on a 4–12% acrylamide gel (Criterion, Hercules, CA, USA) before being transferred to a nitrocellulose membrane for 3 h at 400 mA. Membranes were blocked for at least 1 h in 3% bovine serum albumin (BSA), before being incubated in primary antibody diluted in 3% BSA overnight at 4°C or for 4 h at room temperature. The primary antibodies used in this study were mouse anti-human PTEN (Cascade Biosciences, Winchester, MA, USA, 1 : 5000), rabbit anti-HSP 90 (Cell Signaling, 1:5000), rabbit anti-phosphorylated-ERK1/2 (Cell Signaling, 1:2000), rabbit anti-total ERK1/2 (Cell Signaling, 1:2000), rabbit anti-total AKT (Cell Signaling, 1:2000), rabbit anti-phosphorylated AKT (Cell Signaling, 1:250), mouse anti-Gfap (Santa Cruz, Santa Cruz, CA, USA, 1:10 000) and rabbit anti-GAPDH (Cell Signaling, 1:20 000). Fluorescent secondary antibodies (IR Dye Goat Anti-Rabbit 680 and Goat Anti-Mouse 800, LI-COR Biosciences, Lincoln, NE, USA) were used at a concentration of 1:20 000, and membranes were incubated for at least 1 h at room temperature. Membranes were imaged and band intensity analysis was performed using LI-COR Odyssey or Image Studio software.

Quantitative PCR

Forty-eight microliters per sample of total RNA isolated using the RNeasy kit (Qiagen, Valencia, CA, USA) was DNase treated with the TURBO DNase Kit (Ambion, Grand Island, NY, USA), and the resulting concentration was determined on a Nanodrop 1000. Two micrograms of purified RNA was then reverse transcribed using the Superscript III kit (Invitrogen, Grand Island, NY, USA). Quantitative PCR for *Pten* and *Gapdh* was performed via TaqMan assay (Invitrogen) with triplicate reactions using 20 ng of RNA/reaction. Samples from five mice per genotype were used.

Nissl and Golgi staining

Nissl staining was performed by staining free floating sections in 0.1% cresyl violet solution for 10 min, dipping in 70% ethanol,

and then differentiating in 95% ethanol for 1 min. Golgi staining was performed using the FD Rapid GolgiStain Kit (FD Neurotechnologies, Columbia, MD, USA) according to the manufacturer's protocol. The tissue was sagittally sectioned at 80 μm, and cell morphology analysis was completed using ImageJ (National Institute of Health, Bethesda, MD, USA), focusing on cell body size, dendritic diameter and dendritic spine density. An investigator blinded to genotype performed all image analysis. All experiments used tissue sections from five animals per genotype.

To measure soma size, the circumference of each cell body was manually traced and the cross-sectional area of each cell was recorded. Soma sizes were calculated from 20 to 45 cells/mouse for cortical layer V pyramidal cells, 15–20 cells/mouse for CA1 pyramidal cells, 15–25 cells/mouse for dentate granule neurons and 10 cells/mouse for cerebellar granule cells. Dendritic morphology analysis was performed in CA1 pyramidal neurons, and dendritic diameter was recorded by measuring the diameter of secondary dendrites 30 μm from the apical dendrite. Diameter was based on the average of three measurements per dendritic process and was found for three secondary dendrites per cell, using four cells per animal.

Behavioral tests

All mice, both male and female, used in behavioral experiments were age-matched littermates between P30 and P60. We performed the analyses with this age range to capture a developmental stage when brain development is largely complete but the animals are not yet fully adult.

Sociability

The three-chamber sociability test was performed as previously described (33). Mice were habituated to the center chamber for 5 min, and returned to their home cage. The preference trial consisted of a 10-min trial where the test mouse was given a choice between identical containers with or without a novel mouse inside. Stimulus mice were of the CD-1 genetic background and sex-matched to the test mouse. In order to measure preference for social novelty, the 10-min trial was repeated 2 days later with the familiar mouse and a new mouse instead of an empty container. Time spent in each chamber and time spent in close contact with the containers were recorded using Noldus EthoVision software (Wageningen, Netherlands).

Novel object recognition

Test animals were habituated to the arena for 30 min on day 1, and exposed to two identical objects for 10 min on day 3. After a 24-h delay, the animals were exposed to one familiar and one novel object for 10 min, and time spent with each object was recorded using Noldus EthoVision software (53). The recognition index for each test animal was calculated from object interactions observed during the first 15 s of the trial, in order to capture the time of strongest preference for the novel object prior to habituation (54).

Nociception

Test animals were restrained in a plastic tube and the tail exposed to a halogen lamp heat source until the first tail movement was detected or up to 10 s (55). Average latency to tail flick was calculated from three-trials per mouse.

Open field

The open field test was performed according to the standard protocols (56). Briefly, mice were introduced to the field and allowed to explore for 30 min while the investigator stayed behind a curtain. At the end of the trial, mice were returned to their home cage. Locomotion was measured as the total number of infrared beams broken during the trial, and the periphery of the field was defined as the outer two beams, and included 47% of the total area.

Accelerating rotarod

The accelerating rotarod (Rotamex-5, Columbus Instruments, Columbus, OH, USA) was used to measure locomotor coordination. Test animals were trained on the rotarod for 30 s at 4 rpm, prior to the first test trial. The intertrial interval was 20 min. During each test trial, the rotarod accelerated from 4 to 50 rpm over 5 min, and latency to fall was recorded. Animals completed three trials per day for 3 days for a total of nine trials.

Immunofluorescence

Brains were post-fixed in 4% paraformaldehyde for 24 h, and then dehydrated in 30% sucrose before sectioning at 30 μm on a cryostat. Free-floating sections were washed with PBS, and for NeuN (Millipore, Billerica, MA, USA, 1:500), S100b (Dako, Carpinteria, CA, USA, 1:1000), Iba1 (Wako Pure Chemical Industries, Osaka, Japan, 1:500), CC1 (Millipore, 1:50), Ki67 (Abcam, Cambridge, MA, USA, 1:500) and GFAP (Santa Cruz, 1:1000) antigen retrieval was performed by incubating sections for 10 min at 95°C in 10 mM sodium citrate. Sections were blocked in 5% normal goat serum (NGS) in PBS with 0.03% Triton X-100 for at least 1 h before being incubated in primary antibody diluted in blocking solution overnight at 4°C. Afterward, the sections were washed in PBS, then incubated in fluorescent secondary antibodies diluted in blocking solution at a concentration of 1:1000 (Invitrogen AlexaFluor 488 and 568) and washed again before mounting with Vectashield HardSet mounting medium with DAPI (Vector Laboratories, Burlingame, CA, USA). For Olig2 (Millipore, 1:1000), antigen retrieval was omitted, and sections were incubated in 10% Triton X-100 for 30 min before blocking in 10% NGS in 0.3% Triton X-100. Afterward, sections were incubated overnight at 4°C in primary antibody diluted in 3% NGS in 0.3% Triton X-100. Finally, sections were washed, and incubated in secondary antibody diluted in PBS for 1 h. For NG2/Ki67 double labeling, sections were post-fixed for 2 h. Sections were washed with 0.3 M glycine in PBS, followed by antigen retrieval, and incubation in 10% Triton X-100 for 30 min. Sections were blocked in 10% NGS, 3% non-fat dry milk in 0.3% Triton X-100. NG2 (Millipore, 1:250) and Ki67 (BD Pharmingen, Franklin Lakes, NJ, USA, 1:200) were diluted in 3% NGS, 3% non-fat dry milk in 0.3% Triton X-100 and incubated overnight at 4°C, before secondary antibody incubation as described above. Sections were examined with upright fluorescent or confocal microscopy. Data presented in Figure 4A and Figure 5 were collected from one visual field per section, and 1–2 sections per animal. In Figure 5C, cells were counted across the entire cortex of 1–2 coronal sections per animal. Brain samples from three to five mice per genotype were used in these experiments.

Statistical analysis

Data were analyzed using Student's *t*-test, ANOVA with Tukey's multiple comparison test, or the Kruskal–Wallis test with Dunn's multiple comparison test. Values are presented as mean ± SEM.

SUPPLEMENTARY MATERIAL

Supplementary Material is available at *HMG* online.

ACKNOWLEDGEMENTS

We thank the Cleveland Clinic Rodent Behavioral Core and Dr Olga Nicole Kokiko-Cochran for their guidance and technical advice with the behavioral tasks, and Dr Judith Drazba and Yutaro Komuro for additional technical advice and assistance. We also thank Anita Zaremba for technical assistance with neurosphere culture. We are grateful to Drs Bruce Lamb, Hitoshi Komuro, Richard Ransohoff and Bruce Trapp for their helpful discussions. C.E. is the Sondra J. and Stephen R. Hardis Endowed Chair of Cancer Genomic Medicine at the Cleveland Clinic, and is an ACS Clinical Research Professor.

Conflict of Interest statement. None declared.

FUNDING

This work was supported, in part, by the National Institutes of Health (R01CA118989 to C.E.), and a generous gift from Sam H. Miller.

REFERENCES

1. Butler, M.G., Dasouki, M.J., Zhou, X.P., Talebizadeh, Z., Brown, M., Takahashi, T.N., Miles, J.H., Wang, C.H., Stratton, R., Pilarski, R. *et al.* (2005) Subset of individuals with autism spectrum disorders and extreme macrocephaly associated with germline PTEN tumour suppressor gene mutations. *J. Med. Genet.*, **42**, 318–321.
2. Buxbaum, J.D., Cai, G., Chaste, P., Nygren, G., Goldsmith, J., Reichert, J., Anckarsater, H., Rastam, M., Smith, C.J., Silverman, J.M. *et al.* (2007) Mutation screening of the PTEN gene in patients with autism spectrum disorders and macrocephaly. *Am. J. Med. Genet. B Neuropsychiatr. Genet.*, **144B**, 484–491.
3. McBride, K.L., Varga, E.A., Pastore, M.T., Prior, T.W., Manickam, K., Atkin, J.F. and Herman, G.E. (2010) Confirmation study of PTEN mutations among individuals with autism or developmental delays/mental retardation and macrocephaly. *Autism Res.*, **3**, 137–141.
4. Varga, E.A., Pastore, M., Prior, T., Herman, G.E. and McBride, K.L. (2009) The prevalence of PTEN mutations in a clinical pediatric cohort with autism spectrum disorders, developmental delay, and macrocephaly. *Genet. Med.*, **11**, 111–117.
5. Orrico, A., Galli, L., Buoni, S., Orsi, A., Vonella, G. and Sorrentino, V. (2009) Novel PTEN mutations in neurodevelopmental disorders and macrocephaly. *Clin. Genet.*, **75**, 195–198.
6. Fombonne, E., Roge, B., Claverie, J., Courty, S. and Fremolle, J. (1999) Microcephaly and macrocephaly in autism. *J. Autism Dev. Disord.*, **29**, 113–119.
7. Hobert, J.A., Embacher, R., Mester, J.L., Frazier, T.W. 2nd and Eng, C. (2014) Biochemical screening and PTEN mutation analysis in individuals with autism spectrum disorders and macrocephaly. *Eur. J. Hum. Genet.*, **22**, 273–276.
8. Carter, M.T. and Scherer, S.W. (2013) Autism spectrum disorder in the genetics clinic: a review. *Clin. Genet.*, **83**, 399–407.
9. Zhou, X.P., Marsh, D.J., Morrison, C.D., Chaudhury, A.R., Maxwell, M., Reifenberger, G. and Eng, C. (2003) Germline inactivation of PTEN and dysregulation of the phosphoinositol-3-kinase/Akt pathway cause human Lhermitte-Duclos disease in adults. *Am. J. Hum. Genet.*, **73**, 1191–1198.
10. Tan, M.H., Mester, J., Peterson, C., Yang, Y., Chen, J.L., Rybicki, L.A., Milas, K., Pederson, H., Remzi, B., Orloff, M.S. *et al.* (2011) A clinical scoring system for selection of patients for PTEN mutation testing is proposed on the basis of a prospective study of 3042 probands. *Am. J. Hum. Genet.*, **88**, 42–56.
11. Maehama, T. and Dixon, J.E. (1998) The tumor suppressor, PTEN/MMAC1, dephosphorylates the lipid second messenger, phosphatidylinositol 3, 4, 5-trisphosphate. *J. Biol. Chem.*, **273**, 13375–13378.
12. Page, D.T., Kuti, O.J., Prestia, C. and Sur, M. (2009) Haploinsufficiency for Pten and Serotonin transporter cooperatively influences brain size and social behavior. *Proc. Natl Acad. Sci. USA*, **106**, 1989–1994.
13. Zhou, J., Blundell, J., Ogawa, S., Kwon, C.H., Zhang, W., Sinton, C., Powell, C.M. and Parada, L.F. (2009) Pharmacological inhibition of mTORC1 suppresses anatomical, cellular, and behavioral abnormalities in neural-specific Pten knock-out mice. *J. Neurosci.*, **29**, 1773–1783.
14. Amiri, A., Cho, W., Zhou, J., Birnbaum, S.G., Sinton, C.M., McKay, R.M. and Parada, L.F. (2012) Pten deletion in adult hippocampal neural stem/progenitor cells causes cellular abnormalities and alters neurogenesis. *J. Neurosci.*, **32**, 5880–5890.
15. Kwon, C.H., Luikart, B.W., Powell, C.M., Zhou, J., Matheny, S.A., Zhang, W., Li, Y., Baker, S.J. and Parada, L.F. (2006) Pten regulates neuronal arborization and social interaction in mice. *Neuron*, **50**, 377–388.
16. Wing, L. and Gould, J. (1979) Severe impairments of social-interaction and associated abnormalities in children—epidemiology and classification. *J. Autism Dev. Disord.*, **9**, 11–29.
17. Carpenter, L.A., Soorya, L. and Halpern, D. (2009) Asperger's syndrome and high-functioning autism. *Pediatr. Ann.*, **38**, 30–35.
18. Jaworski, J., Spangler, S., Seeburg, D.P., Hoogenraad, C.C. and Sheng, M. (2005) Control of dendritic arborization by the phosphoinositide-3′-kinase-Akt-mammalian target of rapamycin pathway. *J. Neurosci.*, **25**, 11300–11312.
19. Marino, S., Krimpenfort, P., Leung, C., van der Korput, H.A., Trapman, J., Camenisch, I., Berns, A. and Brandner, S. (2002) PTEN is essential for cell migration but not for fate determination and tumourigenesis in the cerebellum. *Development*, **129**, 3513–3522.
20. Fraser, M.M., Zhu, X., Kwon, C.H., Uhlmann, E.J., Gutmann, D.H. and Baker, S.J. (2004) Pten loss causes hypertrophy and increased proliferation of astrocytes *in vivo*. *Cancer Res.*, **64**, 7773–7779.
21. Harrington, E.P., Zhao, C., Fancy, S.P., Kaing, S., Franklin, R.J. and Rowitch, D.H. (2010) Oligodendrocyte PTEN is required for myelin and axonal integrity, not remyelination. *Ann. Neurol.*, **68**, 703–716.
22. Lobo, G.P., Waite, K.A., Planchon, S.M., Romigh, T., Nassif, N.T. and Eng, C. (2009) Germline and somatic cancer-associated mutations in the ATP-binding motifs of PTEN influence its subcellular localization and tumor suppressive function. *Hum. Mol. Genet.*, **18**, 2851–2862.
23. Trotman, L.C., Wang, X., Alimonti, A., Chen, Z., Teruya-Feldstein, J., Yang, H., Pavletich, N.P., Carver, B.S., Cordon-Cardo, C., Erdjument-Bromage, H. *et al.* (2007) Ubiquitination regulates PTEN nuclear import and tumor suppression. *Cell*, **128**, 141–156.
24. Lobo, G.P., Waite, K.A., Planchon, S.M., Romigh, T., Houghton, J.A. and Eng, C. (2008) ATP modulates PTEN subcellular localization in multiple cancer cell lines. *Hum. Mol. Genet.*, **17**, 2877–2885.
25. He, X., Ni, Y., Wang, Y., Romigh, T. and Eng, C. (2011) Naturally occurring germline and tumor-associated mutations within the ATP-binding motifs of PTEN lead to oxidative damage of DNA associated with decreased nuclear p53. *Hum. Mol. Genet.*, **20**, 80–89.
26. Chung, J.H. and Eng, C. (2005) Nuclear-cytoplasmic partitioning of phosphatase and tensin homologue deleted on chromosome 10 (PTEN) differentially regulates the cell cycle and apoptosis. *Cancer Res.*, **65**, 8096–8100.
27. Chung, J.H., Ginn-Pease, M.E. and Eng, C. (2005) Phosphatase and tensin homologue deleted on chromosome 10 (PTEN) has nuclear localization signal-like sequences for nuclear import mediated by major vault protein. *Cancer Res.*, **65**, 4108–4116.
28. Mester, J.L., Tilot, A.K., Rybicki, L.A., Frazier, T.W. 2nd and Eng, C. (2011) Analysis of prevalence and degree of macrocephaly in patients with germline PTEN mutations and of brain weight in Pten knock-in murine model. *Eur. J. Hum. Genet.*, **19**, 763–768.
29. Kazdoba, T.M., Sunnen, C.N., Crowell, B., Lee, G.H., Anderson, A.E. and D'Arcangelo, G. (2012) Development and characterization of NEX- Pten, a

novel forebrain excitatory neuron-specific knockout mouse. *Dev. Neurosci.*, **34**, 198–209.
30. Baio, J. (2012) Prevalence of autism spectrum disorders—autism and developmental disabilities monitoring network, 14 sites, United States, 2008. *MMWR Surveill. Summ.*, **61**, 1–19.
31. Kwon, C.H., Zhu, X., Zhang, J., Knoop, L.L., Tharp, R., Smeyne, R.J., Eberhart, C.G., Burger, P.C. and Baker, S.J. (2001) Pten regulates neuronal soma size: a mouse model of Lhermitte-Duclos disease. *Nat. Genet.*, **29**, 404–411.
32. Constantino, J.N. and Todd, R.D. (2003) Autistic traits in the general population: a twin study. *Arch. Gen. Psychiatry*, **60**, 524–530.
33. Yang, M., Silverman, J.L. and Crawley, J.N. (2011) Automated three-chambered social approach task for mice. *Curr. Protoc. Neurosci.*, Chapter 8, Unit 8 26.
34. Zbuk, K.M. and Eng, C. (2007) Cancer phenomics: RET and PTEN as illustrative models. *Nat. Rev. Cancer*, **7**, 35–45.
35. Travers, B.G., Powell, P.S., Klinger, L.G. and Klinger, M.R. (2013) Motor difficulties in autism spectrum disorder: linking symptom severity and postural stability. *J. Autism Dev. Disord.*, **43**, 1568–1583.
36. Busch, R.M., Chapin, J.S., Mester, J., Ferguson, L., Haut, J.S., Frazier, T.W. and Eng, C. (2013) Cognitive characteristics of PTEN hamartoma tumor syndromes. *Genet. Med.*, **15**, 548–553.
37. Bonde, E. (2000) Comorbidity and subgroups in childhood autism. *Eur. Child Adolesc. Psychiatry*, **9**, 7–10.
38. Ghaziuddin, M. (2008) Defining the behavioral phenotype of Asperger syndrome. *J. Autism Dev. Disord.*, **38**, 138–142.
39. Eagle, R.F., Romanczyk, R.G. and Lenzenweger, M.F. (2010) Classification of children with autism spectrum disorders: a finite mixture modeling approach to heterogeneity. *Res. Autism Spect. Dis.*, **4**, 772–781.
40. Luikart, B.W., Schnell, E., Washburn, E.K., Bensen, A.L., Tovar, K.R. and Westbrook, G.L. (2011) Pten knockdown *in vivo* increases excitatory drive onto dentate granule cells. *J. Neurosci.*, **31**, 4345–4354.
41. Sperow, M., Berry, R.B., Bayazitov, I.T., Zhu, G., Baker, S.J. and Zakharenko, S.S. (2011) Phosphatase and tensin homologue (PTEN) regulates synaptic plasticity independently of its effect on neuronal morphology and migration. *J. Physiol.*, **590**, 777–792.
42. Flores, A.I., Narayanan, S.P., Morse, E.N., Shick, H.E., Yin, X., Kidd, G., Avila, R.L., Kirschner, D.A. and Macklin, W.B. (2008) Constitutively active Akt induces enhanced myelination in the CNS. *J. Neurosci.*, **28**, 7174–7183.
43. Guardiola-Diaz, H.M., Ishii, A. and Bansal, R. (2012) Erk1/2 MAPK and mTOR signaling sequentially regulates progression through distinct stages of oligodendrocyte differentiation. *Glia*, **60**, 476–486.
44. Bonaguidi, M.A., Wheeler, M.A., Shapiro, J.S., Stadel, R.P., Sun, G.J., Ming, G.L. and Song, H. (2011) *In vivo* clonal analysis reveals self-renewing and multipotent adult neural stem cell characteristics. *Cell*, **145**, 1142–1155.
45. Sofroniew, M.V. and Vinters, H.V. (2010) Astrocytes: biology and pathology. *Acta Neuropathol.*, **119**, 7–35.
46. Franklin, R.J., Bayley, S.A., Milner, R., Ffrench-Constant, C. and Blakemore, W.F. (1995) Differentiation of the O-2A progenitor cell line CG-4 into oligodendrocytes and astrocytes following transplantation into glia-deficient areas of CNS white matter. *Glia*, **13**, 39–44.
47. Windrem, M.S., Nunes, M.C., Rashbaum, W.K., Schwartz, T.H., Goodman, R.A., McKhann, G. 2nd, Roy, N.S. and Goldman, S.A. (2004) Fetal and adult human oligodendrocyte progenitor cell isolates myelinate the congenitally dysmyelinated brain. *Nat. Med.*, **10**, 93–97.
48. Zhu, Y., Romero, M.I., Ghosh, P., Ye, Z., Charnay, P., Rushing, E.J., Marth, J.D. and Parada, L.F. (2001) Ablation of NF1 function in neurons induces abnormal development of cerebral cortex and reactive gliosis in the brain. *Genes Dev.*, **15**, 859–876.
49. Vargas, D.L., Nascimbene, C., Krishnan, C., Zimmerman, A.W. and Pardo, C.A. (2005) Neuroglial activation and neuroinflammation in the brain of patients with autism. *Ann. Neurol.*, **57**, 67–81.
50. Morgan, J.T., Chana, G., Pardo, C.A., Achim, C., Semendeferi, K., Buckwalter, J., Courchesne, E. and Everall, I.P. (2010) Microglial activation and increased microglial density observed in the dorsolateral prefrontal cortex in autism. *Biol. Psychiatry*, **68**, 368–376.
51. Rodriguez-Escudero, I., Oliver, M.D., Andres-Pons, A., Molina, M., Cid, V.J. and Pulido, R. (2011) A comprehensive functional analysis of PTEN mutations: implications in tumor- and autism-related syndromes. *Hum. Mol. Genet.*, **20**, 4132–4142.
52. Redfern, R.E., Daou, M.C., Li, L., Munson, M., Gericke, A. and Ross, A.H. (2010) A mutant form of PTEN linked to autism. *Protein Sci.*, **19**, 1948–1956.
53. Bevins, R.A. and Besheer, J. (2006) Object recognition in rats and mice: a one-trial non-matching-to-sample learning task to study 'recognition memory'. *Nat. Protoc.*, **1**, 1306–1311.
54. Antunes, M. and Biala, G. (2012) The novel object recognition memory: neurobiology, test procedure, and its modifications. *Cogn. Process.*, **13**, 93–110.
55. Lariviere, W.R., Wilson, S.G., Laughlin, T.M., Kokayeff, A., West, E.E., Adhikari, S.M., Wan, Y. and Mogil, J.S. (2002) Heritability of nociception. III. Genetic relationships among commonly used assays of nociception and hypersensitivity. *Pain*, **97**, 75–86.
56. Mehta, M.V., Gandal, M.J. and Siegel, S.J. (2011) mGluR5-antagonist mediated reversal of elevated stereotyped, repetitive behaviors in the VPA model of autism. *PLoS ONE*, **6**, e26077.